

HI-to-H₂ TRANSITION LAYERS IN THE STAR-FORMING REGION W43

SHMUEL BIALY^{*1}, SIMON BIHR², HENRIK BEUTHER², THOMAS HENNING², AND AMIEL STERNBERG¹

Draft version March 11, 2021

ABSTRACT

The process of atomic-to-molecular (HI-to-H₂) gas conversion is fundamental for molecular-cloud formation and star formation. 21 cm observations of the star-forming region W43 revealed extremely high HI column densities, of 120-180 M_⊙ pc⁻², a factor of 10-20 larger than predicted by HI-to-H₂ transition theories. We analyze the observed HI with an HI-to-H₂ transition theoretical model, and show that the theory-observation discrepancy cannot be explained by the intense radiation in W43, nor by variations of the assumed volume density or H₂ formation-rate coefficient. We show that the large observed HI columns are naturally explained by several (9 – 22) HI-to-H₂ transition layers, superimposed along the sightlines of W43. We discuss other possible interpretations such as a non-steady-state scenario, and inefficient dust absorption. The case of W43 suggests that HI thresholds reported in extra-galactic observations are probably not associated with a single HI-to-H₂ transition, but are rather a result of several transition layers (clouds) along the sightlines, beam-diluted with diffuse inter-cloud gas.

Subject headings: galaxies: star-formation – ISM: clouds – ISM: structure – photon-dominated region (PDR)
– ISM: individual objects (W43)

1. INTRODUCTION

The transition of interstellar gas from atomic (HI) to molecular (H₂) form is of fundamental importance for the process of star formation, and has been studied via analytic modeling (e.g., Federman et al. 1979; Sternberg & Dalgarno 1989; Goldsmith et al. 2007; Krumholz et al. 2008; McKee & Krumholz 2010; Sternberg et al. 2014; Liszt 2015; Bialy & Sternberg 2016), hydrodynamical simulations (e.g., Robertson & Kravtsov 2008; Gnedin et al. 2009; Lagos et al. 2015; Valdivia et al. 2016) and observations (e.g., Savage et al. 1977; Reach et al. 1994; Gillmon et al. 2006; Lee et al. 2012; Noterdaeme et al. 2016).

Motte et al. (2014, hereafter M14) and Bihr et al. (2015, hereafter B15) studied the HI and H₂ gas in the W43 star-forming complex. W43 ($l = 29.2 - 31.5^\circ$, $|b| \leq 1^\circ$) is a very active star-formation region, containing many molecular clouds as well as atomic gas, with a total atomic plus molecular gas mass of $\sim 10^7 M_\odot$ (Motte et al. 2003; Nguyễn Luong et al. 2011; Carlhoff et al. 2013; B15). Based on parallax measurements of water and methanol masers, the distance to W43 is $d = 5.5 \pm 0.5$ kpc (Zhang et al. 2014), placing it at the intersection of the Galactic bar with the first spiral arm (Nguyễn Luong et al. 2011).

B15 reported on extremely large HI column densities, $\Sigma_{\text{HI,obs}} 120 - 180 M_\odot \text{pc}^{-2}$, in W43. As shown by M14 and B15, the observed HI columns strongly exceed the columns theoretically expected from single cloud HI-to-H₂ transition models. In such models (e.g., Krumholz et al. 2009; hereafter K09, McKee & Krumholz 2010, and Sternberg et al. 2014; hereafter S14), the HI-to-H₂ transitions are computed assuming a balance between far-UV photodissociation and molecular formation, and accounting for the rapid attenuation of the radiation field due to H₂ self-shielding and dust absorption.

For solar metallicity, the maximal predicted HI columns are $\sim 10 M_\odot \text{pc}^{-2}$, far less than observed in W43.

In this paper we analyze the HI columns in W43. We employ the S14 analytic model for the equilibrium HI columns produced in the transition layers, as functions of the field intensity, gas density, grain properties and metallicity. The S14 and K09 models are very similar in their predictions for the HI columns (see §4 in S14 for a comparison of the planar versus spherical geometry). We show that the simplest and most likely explanation for the large observed HI columns is that several HI-to-H₂ transition layers are superimposed along the sightlines. This possible interpretation was already noted by M14.

The structure of the paper is as follows. We present the observations in §2. In §3 we analyze the data and estimate the number of HI-to-H₂ transition layers. We discuss the implications of our analysis and alternative scenarios in §4. We conclude in §5.

2. OBSERVATIONS

The analyzed HI data is based on observations of “the HI, OH, Recombination line survey of the Milky Way” (THOR; B15; Beuther et al. 2016). For the HI column density of W43, it is crucial to correct for 21 cm optical depth, as well as for weak diffuse continuum emission, otherwise the measured HI mass is underestimated by at least a factor of 2.4 (B15). The measured (corrected) HI column density map is shown in the left panel of Fig. 1. The HI column density typically ranges between 120 and 180 M_⊙ pc⁻². We note, that the corrected HI column density does not decrease toward the center as reported by previous studies (Nguyễn Luong et al. 2011), assuming optically thin HI emission. The molecular gas, as inferred from dust observations is shown in the right panel of Fig. 1 (Nguyễn Luong et al. 2013). It is much clumpier than the HI, and may be decomposed into ~ 20 sub-clouds (Carlhoff et al. 2013). The H₂ column densities typically range within $\sim 100 - 500 M_\odot \text{pc}^{-2}$ with peak values reaching $\sim 3000 M_\odot \text{pc}^{-2}$ at the cores (Nguyễn Luong et al. 2013, Carlhoff et al. 2013, B15).

^{*}shmuebi@mail.tau.ac.il

¹Raymond and Beverly Sackler School of Physics & Astronomy, Tel Aviv University, Ramat Aviv 69978, Israel

²Max Planck Institute for Astronomy, Königstuhl 17, 69117 Heidelberg, Germany

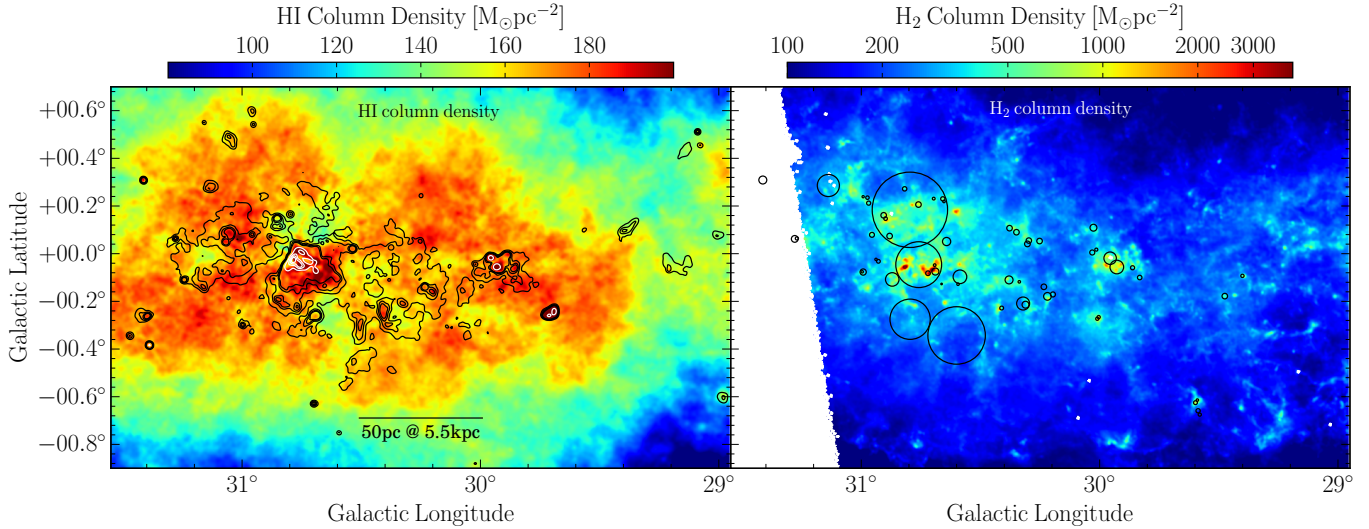


FIG. 1.— Left panel: HI column density taken from [Bihl et al. \(2015\)](#), corrected for optical depth effects and the continuum emission. The contours indicate the 1.4 GHz continuum emission (black contours: 10, 30 and 70 K, white contours: 200, 400, 600 and 800 K). Right panel: H₂ column density, based on Herschel dust observations from [Nguyen-Luong et al. \(2013\)](#). The black circles indicate HII regions taken from [Anderson et al. \(2014\)](#).

To appreciate the high level of star formation activity in the region, the white circles in the right panel of Fig. 1 indicate HII regions, taken from the [Anderson et al. \(2014\)](#) catalog, having distance estimates consistent with W43 ($d \approx 4 - 8$ kpc). The contours in the left panel indicate the 1.4 GHz continuum emission. The relatively high dust temperatures $T_{\text{dust}} \approx 23 - 27$ K (higher than typical $T_{\text{dust}} \lesssim 20$ K; [Reach et al. 1995](#); [Draine 2011](#)) reported by [Nguyen-Luong et al. \(2013\)](#), also suggest intense far-UV irradiation (see §3.1).

3. ANALYSIS

We analyze the observed HI column densities in W43, using the [S14](#) steady-state HI-to-H₂ transition model. The [S14](#) model assumes optically thick, uniform-density slabs, irradiated by beamed or uni-directional far-UV flux. For a two sided slab and isotropic irradiation, the HI column density is

$$\Sigma_{\text{HI}} = \frac{6.71}{\tilde{\sigma}_g} \ln \left(\frac{\alpha G}{3.2} + 1 \right) M_{\odot} \text{ pc}^{-2}, \quad (1)$$

where $\tilde{\sigma}_g \equiv \sigma_g / (1.9 \times 10^{-21} \text{ cm}^2)$ is the dust absorption cross section per hydrogen nucleus in the Lyman-Werner (LW) dissociation band (11.2-13.6 eV), normalized to a fiducial Galactic value (i.e., typically $\tilde{\sigma}_g \approx 1$), α is the ratio of the unshielded H₂ dissociation rate to H₂ formation rate, and G is an average H₂-self shielding factor in dusty clouds (see [S14](#), and [Bialy & Sternberg 2016](#) for a thorough discussion). For a [Draine \(1978\)](#) interstellar radiation spectrum shape, and H₂ formation on dust grains

$$\alpha G = 2.0 I_{\text{UV}} \left(\frac{30 \text{ cm}^{-3}}{n} \right) \left(\frac{9.9}{1 + 8.9 \tilde{\sigma}_g} \right)^{0.37}. \quad (2)$$

Here n is the volume density and I_{UV} is the interstellar radiation intensity relative to the [Draine \(1978\)](#) field. For typical cold neutral medium (CNM) conditions, $\alpha G \approx 2.6$, and is weakly dependent on $\tilde{\sigma}_g$ ([Bialy & Sternberg 2016](#)). Importantly, Eq. (1) is for a *single* two-sided slab (an HI-H₂-HI “sandwich”, hereafter referred by “HI-to-H₂ transition layer”).

Given the large extent of W43 ($\sim 100 \times 200$ pc), the wealth of molecular structures and the many embedded radiation

sources (Fig. 1, [Carlhoff et al. 2013](#)), we argue that the observed HI gas is probably not attributed to a single HI-to-H₂ transition layer but is composed of several transition layers, superimposed along the W43 sightlines. The idea of several transition layers is further supported by the HI spectrum which shows several distinct peaks (see Fig. 10 in [B15](#)), and also by observations of [C II] 158 μm emission ([Shibai et al. 1991](#), as further discussed in §4). The HI spectrum saturates at an optical depth of ~ 3 , and deeper observations of W43 are expected to reveal more structures. In §4 we also discuss alternative scenarios for the large observed HI columns in W43.

Assuming \mathcal{N} transition layers along a sightline, the observed HI column density is given by

$$\Sigma_{\text{HI,obs}} = \phi \mathcal{N} \Sigma_{\text{HI}}, \quad (3)$$

where ϕ is a geometrical factor of order unity, and Σ_{HI} is the column density of a single HI-to-H₂ transition layer as given by Eq. (1). Assuming that the HI-to-H₂ transition layers are slabs that are randomly oriented, $\phi = 1$. This is because a slab that is tilted by an angle θ relative to the plane of the sky, will have a column density $\propto 1/\cos(\theta)$, but will also have an area filling factor $\propto \cos(\theta)$.

In Fig. 2 we plot Σ_{HI} as a function of αG as given by Eq. (1). Overplotted are the observed $\Sigma_{\text{HI,obs}} \approx 120 - 180 M_{\odot} \text{ pc}^{-2}$ (horizontal strip). The vertical strip is the realistic αG range estimated for W43 (see §3.1). Fig. 2 (and Eq. 1) shows that for a single cloud model to fit the observations, unrealistically large values of αG are required. This remained an unresolved puzzle in [B15](#). In the rest of this section we estimate αG and obtain the mean HI column for a single transition layer in W43. We then constrain the number of transition layers along the sightlines using the observed HI columns combined with Eq. (3).

3.1. αG in W43

To constrain αG in W43, we should approximate the UV intensity I_{UV} and the volume density n for the HI gas of W43 (see Eq. 2). Adopting $T_{\text{dust}} = 23 - 27$ K (§2), and assuming thermal equilibrium for the dust grains, $I_{\text{UV}} = (T_{\text{dust}}/T_0)^6$ with $T_0 = 17.5$ K ([Draine 2011](#)), we obtain $I_{\text{UV}} = 5.2 - 13.5$. The modeling of the dust temperature is uncertain to within a fac-

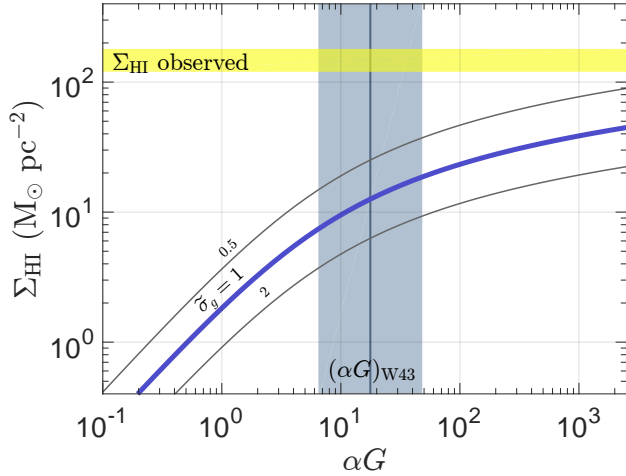


FIG. 2.— The HI column density of a single HI-to-H₂ transition layer as a function of the αG parameter, as given by Eq. (1) assuming $\tilde{\sigma}_g = 1$ (wide blue curve) and factor of two variations about $\tilde{\sigma}_g = 1$ (thin gray). The vertical line and shaded strip are the median αG and the 68.3% range (i.e. “1-sigma” error) for W43. The observed $\Sigma_{\text{HI,obs}}$ in W43 (yellow shading) are larger by factors of $\sim 10 - 20$ than the theoretical curve.

tor of ~ 2 , therefore we consider a wider range for I_{UV} , and adopt $I_{\text{UV}} = 3 - 30$.

We shall now obtain an approximation of the volume density n . Theoretically, the cold neutral medium (CNM; $n \approx 30 \text{ cm}^{-3}$; [Draine 2011](#)), is expected to dominate the shielding and the HI-to-H₂ transition ([K09](#), although see [Bialy et al. 2015](#)). For a CNM gas at thermal equilibrium with warm neutral medium (WNM), the volume density of the CNM is an increasing function of I_{UV} ([Wolfire et al. 2003](#)). For $I_{\text{UV}} = 3 - 30$, [Wolfire et al. \(2003\)](#) suggest $n \sim 30 - 100 \text{ cm}^{-3}$. From an observational point of view, by averaging the observed HI column densities over elliptical annuli and dividing by the equivalent radius, [B15](#) estimated $n \approx 10 - 20 \text{ cm}^{-3}$ for the HI gas in W43. This procedure assumes a uniform density gas. For a clumpy medium the HI density values will increase. In summary, given the uncertainties, we adopt $n = 10 - 100 \text{ cm}^{-3}$ for the atomic gas of W43.

We use Eq. (2) and evaluate the αG probability distribution function (PDF) assuming that $\log n$ and $\log I_{\text{UV}}$ are uniformly distributed within the adopted ranges, giving

$$(\alpha G)_{\text{W43}} = 17.7_{-11.2}^{+30.8} \quad (4)$$

for the median αG and the “1-sigma” error (see Appendix). The median and 1-sigma range are shown by the vertical line and shading in Fig. 2. This αG was evaluated at $\tilde{\sigma}_g = 1$. Although the value of αG depends on the assumed $\tilde{\sigma}_g$, the dependence is weak so for the case of simplicity we show the αG ranges only for $\tilde{\sigma}_g = 1$.

3.2. The number of HI-to-H₂ transition layers

Adopting the αG range given by Eq. (4), the column density of a single HI-to-H₂ transition layer is $\Sigma_{\text{HI}} = 13_{-5}^{+6}/\tilde{\sigma}_g \text{ M}_{\odot} \text{ pc}^{-2}$ (Eq. 1). Following Eq. (3), the number of HI-to-H₂ transition layers is

$$\mathcal{N} = 13_{-4}^{+9} \left(\frac{\Sigma_{\text{HI,obs}}}{160 \text{ M}_{\odot} \text{ pc}^{-2}} \right) \tilde{\sigma}_g \quad (5)$$

where $\Sigma_{\text{HI,obs}}$ is an observed HI column. In Eq. (5), the typical dust absorption cross section is $\tilde{\sigma}_g = 1$ (corresponding to $\sigma_g = 1.9 \times 10^{-21} \text{ cm}^2$). The value of $\tilde{\sigma}_g$ depends on the dust-to-gas ratio and the composition and size distribution of the dust grains. The metallicity and the dust-to-gas ratio typically increase with decreasing galactocentric distance, suggesting that $\tilde{\sigma}_g$ is possibly larger by up to a factor of ~ 2 in W43. The value of $\tilde{\sigma}_g$ depends also on the shape of the extinction curve. The fiducial value assumes $R_V \equiv A_V/E(B-V) = 3.1$ (appropriate for diffuse gas $n \sim 100 \text{ cm}^{-2}$), in dense regions ($n \gtrsim 10^3 \text{ cm}^{-3}$) the dust-extinction curve becomes less steep towards the UV, and $\tilde{\sigma}_g$ may decrease by up to a factor of ≈ 2 ([Draine 2003](#)). Assuming a $\tilde{\sigma}_g = 0.5 - 2$ uncertainty range and reevaluating the PDF of αG , Σ_{HI} and \mathcal{N} , we obtain a larger median value and uncertainty range, $\mathcal{N} = 13_{-6}^{+13} (\Sigma_{\text{HI,obs}}/160 \text{ M}_{\odot} \text{ pc}^{-2})$.

Based on this analysis, a typical column density fluctuation in the HI map may be approximated by $\Delta \Sigma_{\text{HI,obs}}/\Sigma_{\text{HI,obs}} \sim 1/\mathcal{N} \approx 5 - 12\%$, arising from sightlines that differ by a single transition layer. These values are in agreement with the observed HI map shown in Fig. 1.

The length-scale of W43 along the line-of-sight may be approximated, through $\Delta z = \lambda_{\text{HI}} \mathcal{N}$, where λ_{HI} is the characteristic HI scale, given by

$$\lambda_{\text{HI}} = 2 \frac{1}{\sigma_g n} = 11.4 \frac{1}{\tilde{\sigma}_g} \left(\frac{30 \text{ cm}^{-3}}{n} \right) \text{ pc}, \quad (6)$$

where the factor of two is for the two sides of the slab. For $\mathcal{N} = 9 - 21$ and $n = 30 \text{ cm}^{-3}$, $\Delta z \sim 100 - 250 \text{ pc}$, comparable to the projected dimensions of W43. This is only a lower limit on Δz since the HI-to-H₂ transition layers may be spatially separated with diffuse atomic and ionized gas.

4. DISCUSSION

We have shown that the observed HI column densities in W43 are naturally explained by a model of $\sim 9 - 21$ HI-to-H₂ transition layers superimposed along the W43 sightlines. Several transition layers are also expected from the clumpy molecular structure revealed by CO and dust, the high star formation activity and wealth of embedded radiation sources.

Several transition layers along the W43 sightlines were also inferred from [C II] 158 μm observations ([Shibai et al. 1991](#)). Assuming thermal balance between [C II] 158 μm cooling and photoelectric heating, ([Shibai et al. 1991](#)) found $\mathcal{N} \sim 5$ (see their §4.4). However, they assumed a different geometry for the clouds (thin shells). To compare with our model, we modify their formula (their third Eq. in §4.4) to match our randomly-oriented-slab geometry³, giving

$$I_{[\text{CII}]} \simeq 5.1 \times 10^{-6} \mathcal{N} I_{\text{UV}} \text{ erg cm}^{-2} \text{ s}^{-1} \text{ sr}^{-1}. \quad (7)$$

[Shibai et al. \(1991\)](#) reported observations of $I_{[\text{CII}]} = 7 \times 10^{-4} \text{ erg cm}^{-2} \text{ s}^{-1} \text{ sr}^{-1}$ implying $\mathcal{N} = 13.7 (I_{\text{UV}}/10)^{-1}$, consistent with our result $\mathcal{N} = 13_{-4}^{+9}$.

4.1. Model and Observational Limitations

The HI map of [B15](#) was obtained by integrating the 21 cm observations over the “complete” velocity range of W43,

³ We divide their prefactor by 2. An additional factor of 1.7 comes from the normalization of the [Habing \(1968\)](#) radiation fields compared to the [Draine \(1978\)](#) field.

$v_{lsr} = 60 - 120 \text{ km s}^{-1}$ (Nguyen Luong et al. 2011). If part of the observed HI gas is unrelated to W43, or is very diffuse and extended, then $\Sigma_{\text{HI,obs}}$ should be decreased, and the value of \mathcal{N} will decrease accordingly. However, even if we consider only half of the observed Σ_{HI} , still several HI-to-H₂ transitions are required.

In contrast to this, $\Sigma_{\text{HI,obs}}$ could also be higher: B15 used the optical depth τ to correct $\Sigma_{\text{HI,obs}}$. As the used absorption spectrum saturates, the measured optical depth is a lower limit and hence $\Sigma_{\text{HI,obs}}$ is a lower limit as well.

The S14 theory assumes chemical equilibrium. The longest time-scale involved is the H₂ formation-time, $\tau_{\text{H}_2} = 1/(2Rn)$, where R is the H₂-formation rate-coefficient. For $R = 3 \times 10^{-17} \text{ cm}^{-3} \text{ s}^{-1}$ and $n = 30 \text{ cm}^{-3}$, $\tau_{\text{H}_2} = 18 \text{ Myr}$. In a turbulent medium the H₂ formation time may be much shorter, $\sim 1 - 2 \text{ Myrs}$ (Glover & Mac Low 2007).

The S14 model assumes a uniform-density gas for the HI shielding envelopes. In real astrophysical environments the gas is highly turbulent, producing large density fluctuations. However, Bialy, Burkhart & Sternberg (in prep) find that even in highly turbulent supersonic gas, the median Σ_{HI} value remains very close to the homogeneous solution given by Eq. (1). Moreover, for large αG the spread in Σ_{HI} is small (typically within a factor of ~ 2).

Eq. (2) for αG assumes a H₂ formation rate coefficient of $R = 3 \times 10^{-17} \text{ cm}^3 \text{ s}^{-1}$ and a Draine (1978) spectrum shape. The value of R is highly uncertain. However, the fact that the dependence of Σ_{HI} on αG is logarithmic (Eq. 1), makes our analysis robust to variations in all parameters entering αG ; the UV intensity, spectrum shape, volume density, H₂ formation rate coefficient and the H₂-self shielding function.

4.2. Alternative explanations for the large HI columns

M14 and B15 analyzed the observed HI-to-H₂ column densities using the K09 equilibrium model and also found that the observed Σ_{HI} values are far in excess to those predicted theoretically. This is not surprising since like the S14 model, the K09 model is also a steady-state model that is applicable to a single cloud. The M14 and the B15 studies proposed alternative explanations for the theory-observations discrepancy.

B15 suggested that the intense UV radiation field in W43 may account for the large observed $\Sigma_{\text{HI,obs}}$. Following Eq. (1) we see that for a single HI-to-H₂ transition to reproduce the observed HI column densities, αG must be extremely large. For example, for $\Sigma_{\text{HI,obs}} = 120 - 180 \text{ M}_{\odot} \text{ pc}^{-2}$, and assuming $\tilde{\sigma}_g = 1$, $\alpha G = 1.9 \times 10^8 - 1.4 \times 10^{12}$ respectively, requiring unrealistically high I_{UV} to density ratios (see Eq. 2).

A single equilibrium transition layer may be consistent with observations if the dust absorption cross section ($\tilde{\sigma}_g$) is significantly reduced. For the 1-sigma αG range, $\tilde{\sigma}_g = 0.05 - 0.11$ reproduce the observed $\Sigma_{\text{HI}} = 160 \text{ M}_{\odot} \text{ pc}^{-2}$. Such low dust absorption cross-sections may be a result of a reduced dust-to-gas ratio or an abnormal population of dust grains which is selectively inefficient in far-UV absorption. However, this is unlikely given the very large deviation from typical ISM values. The effectiveness of dust absorption may also be reduced by dust-gas separation resulting from non-isotropic radiation (Weingartner & Draine 2001). However, the time-scales involved are very long. For $0.1 \mu\text{m}$ grains $t = 100 r_{\text{pc}} \text{ Myr}$, where r_{pc} is the separation length in pc.

M14 identified three velocity gradients in the position-velocity map of W43, possibly indicative of inflowing gas streams. The large HI columns were then interpreted by M14

as dynamically accumulated atomic gas which has not had time yet to convert into H₂. In this scenario the accretion time-scale must be short compared to the H₂ formation time, $\tau_{\text{H}_2} = 1 - 20 \text{ Myr}$ (§4.1), thus requiring a minimum inflow rate of $\dot{M}_{\text{HI}} = 2.7 - 0.15 \text{ M}_{\odot} \text{ yr}^{-1}$ (assuming $M_{\text{HI}} = 2.7 \times 10^6 \text{ M}_{\odot}$; B15). However, M14 were unable to estimate the gas inflow rates. Even if gas streams are present, they may be dense enough to already contain the equilibrium HI/H₂ interfaces, and contribute to the total number $\mathcal{N} \approx 13$, estimated in §3.2.

The alternatives of photodissociated multiple layers versus a non-equilibrium atomic inflow may be distinguished by the presence or absence of infrared (IR) H₂ line emission. In the layers, far-UV radiation not only photodissociates H₂, but also populates excited H₂ rotational-vibrational levels, resulting in energetic cascade and IR emission. In contrast, for an atomic inflow there are no molecules to excite. Thus, our scenario predicts high IR-line emissions, with an integrated flux being proportional to the observed HI column densities (Black & van Dishoeck 1987; Sternberg 1988). Such observations could confirm the predictions of our multi-slab model. To our knowledge, there are no current IR spectra of the H₂ vibrational transitions in W43.

4.3. Comparison to other HI observations

A much less extreme example of enhanced HI columns may be found in the Perseus molecular cloud. Lee et al. (2015) reported $\Sigma_{\text{HI,obs}} \approx 6 - 9 \text{ M}_{\odot} \text{ pc}^{-2}$, and Bialy et al. (2015) showed that these values are 2 to 3 times larger than what is theoretically expected for CNM conditions. Bialy et al. (2015) showed that this discrepancy is alleviated if the HI gas density in Perseus is lower than typical CNM, with $n \approx 2 - 10 \text{ cm}^{-3}$. The analysis of Bialy et al. (2015) assumed a single HI-to-H₂ transition layer. Following the above discussion, a potentially alternative explanation for the ‘‘too-large’’ HI columns in Perseus would be that there are typically two to three HI-to-H₂ transition layers along the Perseus sightlines.

Extragalactic observations often find an HI threshold of $\approx 10 \text{ M}_{\odot} \text{ pc}^{-2}$ (e.g., Bigiel et al. 2008; Schruba et al. 2011). This threshold was explained in the framework of a steady-state HI-to-H₂ transition model (K09). However, while the model applies to a single cloud, the extragalactic observations, having resolutions of $\sim \text{kpc}$, are not able to resolve molecular clouds, and even not large molecular complexes such as W43. Interpreting the HI threshold as an HI-to-H₂ transition is therefore problematic. The HI threshold might be a result of two effects acting in opposite directions, (i) several HI layers along the line of sight that increase the column density, and (ii) beam dilution by diffuse intercloud gas and WNM, that lowers the observed column densities (Parmentier 2016).

5. CONCLUSIONS

The main results of our paper are as follows.

1. The observed HI column densities in W43, $\Sigma_{\text{HI,obs}} = 120 - 180 \text{ M}_{\odot} \text{ pc}^{-2}$ are very large compared to those predicted by equilibrium HI-to-H₂ theories, $\Sigma_{\text{HI}} \sim 10 \text{ M}_{\odot} \text{ pc}^{-2}$ (K09; S14).
2. Realistic variations of the far-UV flux, spectrum shape, volume density, or the H₂ formation rate coefficient, cannot alleviate the theory-observation discrepancy.

3. The large observed $\Sigma_{\text{HI,obs}}$ are naturally explained by our multi-slab model, in which 9 – 21 transition layers are superimposed along the W43 sightlines. CO, dust and [C II] observations also support this model (Shibai et al. 1991).
4. Time-dependent accumulation of HI is not necessary to account for the large HI columns observed. We predict the presence of IR H₂ line emissions from the multiple transition layers, in our picture. Such emissions would be absent for accumulating inflowing atomic gas.
5. The HI threshold often observed in extragalactic observations (e.g. Bigiel et al. 2008) may be a result of tele-

scope beam averaging of (i) large column densities due to many HI clouds along the sightlines, with (ii) additional diffuse low column density gas.

We thank Jouni Kainulainen, Bruce Draine, Simon Glover and Sahar Shahaf for helpful suggestions and fruitful discussions. We thank the referee for helpful comments on our manuscript. SB thanks the MPIA for visitor support where this research was carried out. This work was supported in part by the PBC Israel Science Foundation I-CORE Program grant 1829/12.

APPENDIX

To obtain the PDF of αG , and in particular the median $\alpha G = 17.7_{-11.5}^{+30}$ (Eq. 4), where the error corresponds to the 68.3 percentile about the median (i.e., “1-sigma”), we assume that $\log I_{\text{UV}}$ and $\log(n/\text{cm}^{-3})$ are uniformly distributed within our adopted $I_{\text{UV}} = 3 - 30$ and $n = 10 - 100 \text{ cm}^{-3}$ ranges (§3.1). We have chosen a uniform distribution since it is the maximum entropy distribution. To obtain the PDF of αG , let us introduce the following random variables,

$$X \equiv \log_{10} \left(\frac{I_{\text{UV}}}{3} \right) \quad (1)$$

$$Y \equiv -\log_{10} \left(\frac{n}{100 \text{ cm}^{-3}} \right) \quad (2)$$

$$Z \equiv \log_{10} \left(\frac{\alpha G}{1.8} \right). \quad (3)$$

With these definitions, X and Y are uniformly distributed within the $[0, 1]$ range, and $Z = X + Y$ (assuming Eq. 2 with $\tilde{\sigma}_g = 1$). The PDF of Z is thus a convolution of the X and Y distribution, and results in the symmetric triangular distribution, with a mean of 1 and a standard deviation $1/\sqrt{6}$. This gives $\alpha G = 17.7_{-11.5}^{+30}$ for the median and 68.3 percentile about the median. The 95.5, and 99.7 percentiles correspond to $\alpha G=2.9-108.4$, and $2.0-157.0$, respectively (the ranges are symmetric about the median in log space). The PDF of αG may also be obtained numerically by generating large amounts of random pairs for $\{\log I_{\text{UV}}, \log(n/\text{cm}^{-3})\}$, and then using Eq. (2) to obtain the αG PDF. We have followed such a numerical procedure to verify the above analytic result.

REFERENCES

- Anderson, L. D., Bania, T. M., Balser, D. S., et al. 2014, *ApJS*, 212, 1
 Beuther, H., Bihr, S., Rugel, M., et al. 2016, *A&A*, 595, A32
 Bialy, S., & Sternberg, A. 2016, *ApJ*, 822, 83
 Bialy, S., Sternberg, A., Lee, M.-Y., Le Petit, F., & Roueff, E. 2015, *ApJ*, 809, 122
 Bigiel, F., Leroy, A., Walter, F., et al. 2008, *AJ*, 136, 2846
 Bihr, S., Beuther, H., Ott, J., et al. 2015, *A&A*, 580, A112
 Black, J. H., & van Dishoeck, E. F. 1987, *ApJ*, 322, 412
 Carlhoff, P., Luong, Q. N., Schilke, P., et al. 2013, *A&A*, 560
 Draine, B. T. 1978, *ApJS*, 36, 595
 —. 2003, *ApJ*, 598, 1017
 Draine, B. T. 2011, *Physics of the Interstellar and Intergalactic Medium*, Princeton University Press.
 Federman, S. R., Glassgold, A. E., & Kwan, J. 1979, *ApJ*, 227, 466
 Gillmon, K., Shull, J. M., Tumlinson, J., & Danforth, C. 2006, *ApJ*, 636, 891
 Glover, S. C. O., & Mac Low, M.-M. 2007, *ApJ*, 659, 1317
 Gnedin, N. Y., Tassis, K., & Kravtsov, A. V. 2009, *ApJ*, 697, 55
 Goldsmith, P. F., Li, D., & Krčo, M. 2007, *ApJ*, 654, 273
 Habing, H. J. 1968, *Bull. Astron. Inst. Netherlands*, 19, 421
 Krumholz, M. R., McKee, C. F., & Tumlinson, J. 2008, *ApJ*, 689, 865
 Krumholz, M. R., McKee, C. F., & Tumlinson, J. 2009, *ApJ*, 693, 216
 Lagos, C. d. P., Crain, R. A., Schaye, J., et al. 2015, *MNRAS*, 452, 3815
 Lee, M.-Y., Stanimirović, S., Murray, C. E., Heiles, C., & Miller, J. 2015, *ApJ*, 809, 56
 Lee, M.-Y., Stanimirović, S., Douglas, K. A., et al. 2012, *ApJ*, 748, 75
 Liszt, H. S. 2015, *ApJ*, 799, 66
 McKee, C. F., & Krumholz, M. R. 2010, *ApJ*, 709, 308
 Motte, F., Schilke, P., & Lis, D. C. 2003, *ApJ*, 582, 277
 Motte, F., Nguyen Luong, Q., Schneider, N., et al. 2014, *A&A*, 571
 Nguyễn Luong, Q., Motte, F., Schuller, F., et al. 2011, *A&A*, 529
 Nguyen-Luong, Q., Motte, F., Carlhoff, P., et al. 2013, *ApJ*, 775, 88
 Noterdaeme, P., Krogager, J.-K., Balashev, S., et al. 2016, *A&A* accepted, ArXiv 1609.01422
 Parmentier, G. 2016, *ApJ*, 826, 74
 Reach, W. T., Koo, B.-C., & Heiles, C. 1994, *ApJ*, 429, 672
 Reach, W. T., Dwek, E., Fixsen, D. J., et al. 1995, *ApJ*, 451, 188
 Robertson, B. E., & Kravtsov, A. V. 2008, *ApJ*, 680, 1083
 Savage, B. D., Bohlin, R. C., Drake, J. F., & Budich, W. 1977, *ApJ*, 216, 291
 Schrubba, A., Leroy, A. K., Walter, F., et al. 2011, *AJ*, 142, 37
 Shibai, H., Okuda, H., Nakagawa, T., et al. 1991, *ApJ*, 374, 522
 Sternberg, A. 1988, *ApJ*, 332, 400
 Sternberg, A., & Dalgarno, A. 1989, *ApJ*, 338, 197
 Sternberg, A., Le Petit, F., Roueff, E., & Le Bourlot, J. 2014, *ApJS*, 790, 10S
 Valdivia, V., Hennebelle, P., Génin, M., & Lesaffre, P. 2016, *A&A*, 587, A76
 Weingartner, J. C., & Draine, B. T. 2001, *ApJ*, 553, 581
 Wolfire, M. G., McKee, C. F., Hollenbach, D., & Tielens, A. G. G. M. 2003, *ApJ*, 587, 278
 Zhang, B., Moscadelli, L., Sato, M., et al. 2014, *ApJ*, 781, 89